Mars Methane Sources in Northwestern Gale Crater Inferred from Back-Trajectory Modeling

Yangcheng Luo
California Institute of Technology https://orcid.org/0000-0003-0983-3650
Michael Mischna
JPL
John Lin
University of Utah
Benjamin Fasoli
University of Utah
Xiang Cai
Santiago High School
Yuk Yung (yly@gps.caltech.edu)
Caltech https://orcid.org/0000-0002-4263-2562

Article

Keywords: Sample Analysis at Mars (SAM), Tunable Laser Spectrometer (TLS), back-trajectory modeling

DOI: https://doi.org/10.21203/rs.3.rs-569847/v1

Abstract

During its five years of operation, the Sample Analysis at Mars (SAM) Tunable Laser Spectrometer (TLS) on board the *Curiosity* rover has detected six methane spikes above a low background abundance in Gale crater. The methane spikes are likely the consequence of nearby surface emission. Here we use inverse Lagrangian modeling techniques to identify probable upstream emission regions for these methane spikes at an unprecedented spatial resolution. Inside Gale crater, the northwestern crater floor casts the strongest influence on the detections. Outside Gale crater, the emission region with the strongest influence extends towards the north. The contrasting results from two consecutive methane measurements point to an active emission region to the west and the southwest of the *Curiosity* rover on the northwestern crater floor. The observed spike magnitude and frequency also favor emission sites on the northwestern crater floor, unless fast methane removal mechanisms that are unknown to date are at work.

Introduction

Almost all of the methane in the present-day Earth's atmosphere can be traced back to biological origins[1]. Extending this observation to Mars, this would suggest that the presence of methane in the Martian atmosphere could be a biosignature on this seemingly lifeless planet[2]. Alternative, abiotic methane production mechanisms on Mars invoke past or present geological activity (reviewed in ref. 3) such as serpentinization[4], which indicates the presence of liquid water, an indispensable ingredient for life. Abundant methane in the ancient Martian atmosphere could also provide a solution to the conflict between the Faint Young Sun and a warm surface suggested by fluvial and lacustrine features on Mars (e.g., ref. 5).

In the past two decades, the significance of methane in the Martian atmosphere has motivated a number of remote sensing observations aimed at retrieving the methane abundance in the Martian atmosphere and mapping out its spatial distribution. They reported inconsistent and highly variable methane concentrations[6, 7, 8, 9, 10, 11, 12, 13]. To overcome the technical challenges faced by remote sensing observations, the Tunable Laser Spectrometer[14] (TLS) on board the *Curiosity* rover was sent to Gale crater to make *in situ* measurements. During 4.6 years of operation through May 2017, twenty direct-ingest measurements and ten enrichment measurements (refer to ref. 15 and ref. 16 for descriptions of the two measurement types) revealed a baseline level of ~ 0.41 parts-per-billion-by-volume (ppbv), with episodic spikes up to ~ 10 ppbv (ref. 16) as summarized in Fig. 1. These spikes have been interpreted as discrete methane emission events[15, 16]. Recently, after one year of operation, the ExoMars Trace Gas Orbiter (TGO) announced an upper limit of 0.06 ppbv for altitudes above 6 km, which has been interpreted as the upper limit for a global background methane concentration under the assumption that methane is a long-lived species[17, 18]. Assuming a 330-year methane lifetime from standard photochemical models[19], methane should be uniformly mixed in the Martian atmosphere, so TGO's result is seemingly contradictory to TLS's significantly more elevated ~ 0.41 ppbv background level. But some mechanisms

have been proposed to reconcile this inconsistency. TLS measurements were all performed in the near-surface planetary boundary layer (PBL), and surface-released methane could accumulate in the shallow nighttime PBL[20, 21]. Some speculative fast removal mechanisms that can possibly cause temporal and spatial inhomogeneity of methane concentration have also been proposed[22, 23, 24].

The origin of methane on Mars has great implications for geology and astrobiology. The identification of the methane origin requires that we first find the surface emission sites of methane, results from which can inform future missions of high priority landing sites and enable them to directly probe the methane source. The results may also guide orbiting instruments to better focus their methane observation strategies.

Inferring emission sites of methane requires correct modeling of complex atmospheric transport processes. An early attempt to do so involved using a diffusion model to represent the spread of observed methane plumes[9], which was shown to be oversimplified by addressing the importance of advection by bulk wind[25]. More recently, the Global Environmental Multiscale (GEM)-Mars general circulation model (GCM) was used to simulate methane transport and then a statistical approach based on the idea of simultaneous satisfaction of multiple observational constraints was used for methane source localization[13]. Results suggested an emission region to the east of Gale crater for Spike 1 in Fig. 1. Later, the Mars Regional Atmospheric Modeling System (MRAMS) model was used to simulate the transport and dispersion of methane plumes emitted from ten selected source regions around Gale crater[26]. Substantial dilution during tracer transport was observed, which demonstrates the importance of incorporating turbulent dispersion into tracer transport modeling. Among all the ten emission region candidates, the region to the northwest of the crater was favored, different from previous findings (e.g., ref. 13).

The aforementioned emission site localization studies all adopted a forward Eulerian approach, in which the model integrates three-dimensional tracer fields forward in time and quantifies how much tracer released at specific emission locations and times can ultimately reach a detector. However, this “trial-and-error” approach is computationally expensive, so usually only a small number of putative emission sites are selected and studied in depth (e.g., ref. 26). Meanwhile, the spatial resolution of emission regions is limited by the size of GCM grid boxes, making it difficult to localize emission sites within Gale crater (e.g., ref. 13). (Refer to the Methods section for more discussions on the challenges faced by the forward Eulerian approach.)

In this work, we adopt an *inverse* Lagrangian approach[27, 28] to overcome the challenges faced by forward Eulerian emission site localization techniques. The inverse Lagrangian approach is also known as back-trajectory analysis and is widely used for emission site localization on Earth. An ensemble of computational particles, representing air parcels, is released from the detector at the time of detection and is transported backwards in time. The particles’ transport pathways are determined by the bulk wind and the particles are dispersed by parameterized subgrid-scale turbulence. The locations where backward-travelling particles are found within the PBL and hence are potentially affected by surface

emission are identified as potential upstream emission regions. The quantitative linkage between measured atmospheric mole fraction at the detector and upstream surface fluxes is established via the number density of particles at an upstream location[27, 29]. A single inverse Lagrangian simulation can quantify the influence of all upstream emission regions on a detected signal, where the spatial resolution of emission regions is not limited by the GCM resolution. As such, high-resolution maps of all probable upstream emission regions can be produced, which is critical for the search for potential emission sites within and around the small, 154-km wide, Gale crater.

Results

Categorization of methane spikes

We focus on the six methane spikes reported by the TLS instrument (which is referred to as the "detector" in the following text) during the 4.6 years of the *Curiosity* mission through May 2017 (Fig. 1, Table S1). The six spikes can be categorized based on the seasons and the time of day of their detections. In terms of seasons, Spikes 1 and 6 were detected from late northern fall into winter. Spikes 2–5 were detected in northern spring. In terms of the time of day, Spikes 1 and 5 were detected in the early afternoon ("daytime"), and Spikes 2, 3, 4 and 6 were detected between midnight and early morning ("nighttime"). As a result, Spikes 1 and 6 share similar seasonal, regional and global circulation patterns, as do Spikes 2–5. Spikes 1 and 5 share similar diurnal crater circulation patterns, as do Spikes 2, 3, 4 and 6. The similarity in atmospheric circulation patterns also manifests itself in the subsequent emission region localization.

Atmospheric circulations

Current understanding of atmospheric circulation in Gale crater is primarily based on GCM and higher-resolution mesoscale simulations. We employ MarsWRF, a Mars GCM and mesoscale model to simulate atmospheric circulation at Gale crater (refer to the Methods section for detailed model configurations). Simulation results show that the circulation consists of three components – a global meridional overturning circulation, a regional circulation, and a crater-scale circulation. Figure 2 shows an example of near-surface winds simulated by MarsWRF. In northern winter, the rising branch of the global meridional overturning circulation is centered in the southern hemisphere. Prevailing winds at the topographic dichotomy next to Gale crater are towards the south and are particularly strong around 270° solar longitude when Spike 6 was detected. In northern spring, the large-scale prevailing winds at Gale crater are weak. The regional circulation is characterized by upslope northerlies along the topographic dichotomy in the afternoon, and downslope southerlies in the nighttime. The crater circulation is characterized by upslope winds along the inner crater rim and the slope of Mount Sharp in the afternoon, and downslope winds in the nighttime. The PBL thickness at Gale crater undergoes a daily cycle between a nighttime minimum thickness of tens of meters, and a daytime maximum thickness of about three kilometers, similar to previous findings in ref. 30.

Upstream emission regions

At every timestep in a back-trajectory simulation (which corresponds to an emission time), based on the instantaneous particle density in the PBL, STILT generates a “footprint” map in units of ppbv μmol^{-1} (ref. 27), which quantifies the contribution of unit methane emission from any emission site at that emission time to the methane mole fraction at the detector. The values of footprints are equal to the prospected methane mole fraction in the unit of ppbv above the ~ 0.41 ppbv background level induced by 1 μmol of methane emission. High footprints at a certain emission time indicate regions where the emission at that emission time casts strong influence over the detection, or in brief, the upstream regions. Time-integrated footprints measure the influence of a constant-flux emission on a detection, which show upstream regions at all possible emission times. Figure 3 shows the time-integrated footprint maps for Spikes 1 and 2. Refer to Fig. 5 and Fig. S5 for the footprints of Spikes 3–6.

Within Gale crater, the strongest footprint of Spike 1 is located to the north of the TLS detector (Fig. 3a), which is also the case for Spike 5 (Fig. S5g). The similarity in their footprints is consistent with the similarity in the early-afternoon crater-scale circulation patterns when these two spikes were detected (Fig. 1, Table S1). Despite the different seasons of these two detections, the prevailing local wind in the early afternoon comes from the north in both cases. For Spike 2, the strongest footprint lies on the entire northwestern crater floor (Fig. 3d), which is also the case for Spikes 3, 4, and 6 (Fig. 5d, Fig. S5a, d), despite some fine spatial patterns in the footprints of Spike 6. These four spikes were all detected in the nighttime when the PBL was shallow. The released particles are confined within the PBL, so they imprint almost equally strong footprints onto the entire northwestern crater floor as they are advected backwards in time. In the time-forward perspective, emission that occurs at different places on the northwestern crater floor in the nighttime casts almost equal influence over a nighttime detection.

Outside Gale crater, the strongest footprint for Spike 1 lies to the north of the crater, as a result of the prevailing northerlies in this season (Fig. 3b). This is also true for Spike 6 (Fig. 5e). This shows that for these two spikes, if a methane emission region exists in the neighborhood of Gale crater (but outside the crater), it is most likely located to the north of the crater. The locations of the upstream regions for Spike 2 are, however, less definitive. The strongest footprints for Spike 2 cover the regions in the first and third quadrants of Gale crater (Fig. 3e). This is also true for Spikes 3–5 (Fig. S5b, e, h). Despite this ambiguity, the strongest footprints for all the six spikes overlap in a region within 300 km to the north of Gale crater. It is noteworthy that the “E8” and “ESE” regions, suggested as the most likely emission regions for Spike 1 (ref. 13), do not bear strong footprints in our study and are hence not identified as the preferred upstream regions for Spike 1 (Fig. 3b).

Further zooming out to the hemispherical scale, the strongest footprints of Spike 1 extend from Elysium Planitia towards two directions – one to the north along the western side of Elysium Mons reaching Utopia Planitia, and the other to the east along the southern side of Elysium Mons reaching Amazonis Planitia (Fig. 3c). This is also true for Spike 6, although the northern branch appears more prominent (Fig. 5f). This suggests that these large-scale geographic units are more likely to be the emission regions than other large-scale geographic units for Spikes 1 and 6. For Spikes 2–5, the strong footprints cover

many large-scale geographic units around Gale crater (Fig. 3f, Fig. S5c, f, i), with the aforementioned Elysium Planitia and Utopia Planitia included.

Minimum methane emission

Based on the footprints, the minimum amount of methane emission from any emission site required by the observed methane spikes can be calculated. TLS's ~ 0.41 ppbv background level is first subtracted from the six methane spikes. The remainder of the signals must then be a consequence of recent emission. It is unknown whether the emission was continuous, intermittent, or episodic, but to put a lower bound on the required methane emission, we can assume the emission was instantaneous and occurred at the exact moment when an emission site had the strongest influence on a detection. Finally, dividing each methane signal by the maximum footprint at an emission site yields the minimum amount of methane emitted from that emission site required by the methane signal (Fig. 4). Regions that can produce the methane signals by emitting a small amount of methane are well correlated with the regions bearing strong footprints in Fig. 3.

TGO's 0.06 ppbv upper limit on the background concentration, combined with the 330-year lifetime from standard photochemical models, implies that, on average, no more than 1.8×10^{-4} ppbv of methane is replenished every year. During the 4.6 years of TLS operation, then, on average, no more than about 8.4×10^{-4} ppbv has been replenished into the atmosphere. Assuming the six methane spikes result from six emission events, then, on average, each of them can emit no more than 1.4×10^{-4} ppbv of methane; otherwise, they would have resulted in a significant, and observable rise in the background methane concentration. Only the blue and cyan areas in Fig. 4 are such qualified areas that are able to produce a methane spike with the observed mole fraction by emitting less than 1.4×10^{-4} ppbv of methane. This means that without fast removal mechanisms that can significantly reduce the methane lifetime, the methane emission site needs to be located within the blue and cyan areas inside Gale crater. In fact, the assumed situation where only six methane emission events occurred during the 4.6 years and all of them were captured by the TLS measurements is almost impossible. The actual emission event frequency may be much higher than this, which will put a much lower upper bound on the amount of methane emitted by a single emission event. The qualified emission regions will then be confined within much smaller areas, such as the blue or even the dark blue areas on the northwestern crater floor in Fig. 4. However, this suggests a coincidence that *Curiosity* was sent to the vicinity of a methane emission hotspot. Another possibility that does not invoke the coincidence is that rapid methane removal mechanisms that are not known to date are at work. If the methane lifetime is shorter than 330 years, more methane can be emitted into the atmosphere every year without perturbing the background methane concentration, and the emission sites will have some freedom to be located at distant places outside Gale crater. (Refer to Fig. S10 for a more thorough analysis.)

Consecutive methane measurements

At ~ 266° solar longitude in Mars Year 33, two measurements were consecutively performed within a few hours. The first measurement started at ~ 01:30 local time and detected a 0.332 ppbv signal. Only a few hours later, the second measurement at ~ 06:30 local time detected Spike 6 with 5.55 ppbv. It is possible

that the rapid increase in the ambient methane concentration is due to the change in wind direction. Figure 5 shows a comparison of the time-integrated footprints for Spike 6 and the background level. A significant difference can be found between the upstream regions within Gale crater (Fig. 5a, d). There are not significant differences between the upstream regions at larger scales (Fig. 5b, e, and Fig. 5c, f). On the northwestern crater floor, the upstream region of Spike 6, indicated by high footprint values, primarily lies to the west and the southwest of *Curiosity* rover, whereas the upstream region of the background level primarily lies to the northeast of the rover. Therefore, the region to the west and the southwest of *Curiosity* in northwestern Gale crater is identified as the most likely location of an emission site.

We note that this method based on consecutive methane measurements is able to precisely constrain the location of an emission site, but it requires consecutive measurements performed within a short period of time, optimally a few hours. Fortunately, the measurement strategy of TLS, which often performs paired measurements within a few hours, meets this requirement.

Concluding remarks

In conclusion, if we trust the methane abundances detected by both TLS and TGO and accept the 330-year methane lifetime from known photochemistry, our back-trajectory modeling for atmospheric transport strongly supports surface emission sites in the vicinity of the *Curiosity* rover in northwestern Gale crater. This may invoke a coincidence that we selected a landing site for *Curiosity* that is located next to an active methane emission site. Another possibility that does not invoke the coincidence is the existence of fast methane removal mechanisms that are unknown to date. Should future studies confirm the existence of heterogeneous pathways or other unknown photochemical processes for methane destruction, the methane emission sites can be located outside Gale crater, and most likely to the north of the crater.

Our study demonstrates the feasibility and the advantages of applying the inverse Lagrangian modeling technique to source localization problems on other planets. Methane abundance data from future *in situ* measurements, especially those collected in consecutive measurements performed within a few hours, would further improve the source localization.

Methods

GCM simulations

Since global, high-quality wind observations on Mars have been lacking to date, we use MarsWRF, a GCM of the Martian atmosphere, to simulate the wind fields necessary for the inverse Lagrangian approach. MarsWRF is derived from the terrestrial WRF model and is a Mars-specific implementation of PlanetWRF[31]. MarsWRF is a finite-difference grid-point model projected onto an Arakawa-C grid with user-defined horizontal and vertical resolutions. The vertical grid follows a modified-sigma (terrain-following) coordinate from the surface to ~ 80 km altitude. The total present-day atmospheric CO_2 budget is tuned to fit the Viking Lander annual pressure curves (~ 6.1 mbar), and both surface albedo and thermal inertia

are matched to Mars Global Surveyor Thermal Emission Spectrometer (MGS-TES) observations[32, 33], while a Mars Orbiter Laser Altimeter (MOLA) topography base map is employed and scaled to the chosen model resolution.

Multiple studies in the past have validated MarsWRF through comparison of its behavior against data from the *Mars Global Surveyor* Thermal Emission Spectrometer[34, 35, 36, 37], the *Mars Reconnaissance Orbiter* Mars Climate Sounder[36], and the weather stations on board *Curiosity*[30, 38] and *InSight*[39], showing MarsWRF reproduces observed wind speeds and directions reasonably well.

MarsWRF permits multiple embedded "nests" with increasing spatial resolutions in a single model run. This allows atmospheric circulations influenced by small-scale topographic features to be fully resolved in a simulation that also covers the entire globe. In this study, we run MarsWRF at increasing horizontal resolutions around Gale crater. The final model consists of four nested levels, each scaled up in resolution (spatial and temporal) by a factor of three. Level 1 provides global coverage with a horizontal resolution of 2°×2° and a 60-second timestep. Level 2 encompasses an 80°×80° domain with a horizontal resolution of 0.67°×0.67° and a 20-second timestep. Level 3 encompasses a 26.67°×26.67° domain with a horizontal resolution of 0.222°×0.222° and a 6.67-second timestep. Level 4 encompasses an 8.89°×8.89° domain with a horizontal resolution of 0.74°×0.74° (4.4 km×4.4 km) and a 2.22-second timestep (Fig. S1), which fully resolve the crater circulation. Two-way boundary conditions link a nested domain with its "parent", with information being passed both up and down between parent and child domains. A description of this process may be found in ref. 31. In order to speed up the simulations, we performed test simulations in advance to determine the duration of simulations on each nesting level, such that a high-level nesting can be turned off after about 99% of the initially released particles have left the domain of that nesting level.

Smoothing out weather variability

Given the lack of a global coverage of high-quality wind observations, it is impossible to reasonably predict precise "real" atmospheric circulations on spatial scales smaller than tens of kilometers, as stochastic weather events can significantly impact wind speed and even direction. As a result, we do not intend to reproduce the "real" winds. Instead, we aim to produce "mean" winds that are representative of their respective seasons and time of day. For each TLS measurement, we repeat MarsWRF simulations five times for five consecutive model years. The five rounds of simulations for each measurement are all driven by the same seasonally representative dust loadings and show slight variations in year-to-year conditions as a consequence of stochastic variability in the weather. The variance in results across the five years is, however, small.

On short timescales (< 1 week), it is not anticipated there will be significant change in mean atmospheric conditions on Mars, and so for each of the five rounds of wind simulations, we treat the sol of measurement, and one, two, three sols before and after the measurement as equally representative of the weather at the time of the TLS measurement, and release ten thousand particles at the time of day of each measurement on all of the seven sols. In this way, we form an ensemble of thirty-five back-trajectory

simulations for each investigated TLS measurement, and the following analysis is all based on the average footprints of these thirty-five simulations. This ensures that discrete weather patterns are smoothed out.

Inverse Lagrangian analysis

The wind fields from MarsWRF are used to drive the Stochastic Time-Inverted Lagrangian Transport (STILT) Lagrangian Particle Dispersion Model[27, 29] to simulate plume transport and dispersion. STILT is based on the Hybrid Single Particle Lagrangian Integrated Trajectory (HYSPLIT) model[40, 41] that is extensively used in air quality, volcanic ash and industrial plume modeling, and STILT inherits all of the validated components of its predecessor. In its application, STILT transports an ensemble of computational particles (ten thousand particles in each simulation in this study) from the site of the detector (here, the location of the *Curiosity* rover) using time-reversed grid-scale wind plus a parameterized subgrid-scale turbulent velocity[42]. The timestep in STILT is determined dynamically based on the wind field, and typically ranges between one minute and ten minutes. At each timestep, STILT linearly interpolates the bulk wind simulated by a GCM from the grid points of the GCM to the precise positions of each particle, and then displaces the particles according to the reversed wind arrow. Meanwhile, STILT adds a random velocity component, determined by a Markov chain process based statistically on GCM-simulated meteorological parameters, to the GCM-simulated bulk wind velocity. The random velocity represents turbulent motions that are unresolved by the GCM, and results in dispersion of the particle cloud (Fig. S3). Additionally, vertical mixing in the PBL is parameterized by vertically redistributing particles to random altitudes within the PBL (Fig. S4). In the hyper-near field around the detector, an “effective mixing depth” smaller than the PBL thickness is calculated based on the homogeneous turbulence theory[29], so that it will take some time for particles released near the surface to ascend to the top of the PBL.

At each timestep, STILT tallies the instantaneous particle density in the PBL at all locations and generates a “footprint” map in units of ppbv μmol^{-1} (ref. 27), which quantifies the contribution of unit methane emission flux from an emission site to the methane mole fraction at the detector. The STILT footprint is proportional to the number density of particles vertically integrated from the surface to the top of the PBL and the molar mass of air, and inversely proportional to the PBL thickness and the average air density within the PBL[27]. The domain is first gridded horizontally (a grid that is separate from that of the GCM) so that STILT can count the number of particles within each horizontal grid and calculate the particle density at all horizontal locations. The resolution of this grid becomes the resolution of the footprints, and hence the resolution of the emission regions. We use 2° as the resolution for the domain from 80°S to 80°N and from 60°E eastward to 140°W. For the subdomain from 17.6°S to 8.4°N and from 124.2°E to 150.4°E, we use a higher resolution of 0.2°, or ~ 11.8 km. For the subdomain from 6.64°S to 3.72°S and from 136.24°E to 139.16°E, we use a further higher resolution of 0.02°, or ~ 1.18 km. We note that the definition of the STILT footprint in this study is slightly different from that in ref. 27. The new definition has excluded the impact of the grid size and the timestep of the footprint calculation on the magnitude of the footprints by dividing the original STILT footprint by the grid size and the timestep.

STILT was originally designed for terrestrial use, and we adapted STILT so that it can be used for Mars. The modifications include changes to planetary radius, gas constant, angular rotation rate of the planet, surface gravity, dynamic viscosity of air, mean free path of air, molecular weight of air, surface air pressure, specific heat capacity of air, the map of land use, and the map of surface roughness length[43], etc. We note that the Monin–Obukhov similarity theory for the PBL, along with the adherence to the well-mixed criterion[44], a manifestation of the second law of thermodynamics, ensures that the physics and fluid dynamics underlying STILT can be applied to all substantial planetary atmospheres, including the Martian atmosphere.

Challenges faced by the classical forward Eulerian approach

The forward Eulerian approach integrates tracer fields forward in time. It quantifies the influence of different emission locations on the detection based on how much tracer released at these locations at different times can ultimately reach the detector. Two methods have been applied. The first method considers a single emission site and a single emission time by releasing tracers from one GCM grid point and at one timestep in each simulation. This method is computationally expensive, as an extensive grid search on a multi-dimensional parameter space spanned by all possible emission sites and times is necessary. This high cost limits the spatial resolution of emission sites to coarse, regional surveys. For example, emission sites inside Gale crater were not resolved in ref. 13. The other method tags tracers from different origins using different tracer indices within a single simulation, and then simulates the evolution of the tracer index field (e.g. ref. 26). While the large number of experiments is circumvented, the spurious grid-scale numerical diffusion demanded by model stability gradually smooths out the tracer index field in a simulation, and ultimately decouples the tracer index from the original location and time of emission, resulting in uncertainty in the search for surface emission sites.

Declarations

Data Availability: The output from the MarsWRF simulations is in the NetCDF format and can be accessed via email to the corresponding author. The original version of the STILT software can be accessed at the Github page https://uataq.github.io/stilt/#/. The STILT code adapted for Mars conditions, along with the output from the Mars STILT model in the RDS format and in the NetCDF format, can be accessed via email to the corresponding author. None of the aforementioned data are subject to any restrictions.

Acknowledgments: A portion of this research was carried out at the Jet Propulsion Laboratory, California Institute of Technology, under contract with NASA. Government sponsorship acknowledged. Y. L. Y acknowledges the President's and Director's Research and Development Fund and the support from the Virtual Planetary Laboratory at the University of Washington that is funded via NASA Astrobiology Program Grant No. 80NSSC18K0829. Resources supporting this work were provided by the NASA High-End Computing (HEC) Program through the NASA Advanced Supercomputing (NAS) Division at Ames Research Center.

Author Contributions:

Conceptualization: YL, MAM, YLY

Methodology: YL, MAM, JCL, BF, YLY

Investigation: YL, MAM

Visualization: YL, XC

Funding acquisition: MAM, YLY

Writing – original draft: YL, MAM

Writing – review & editing: MAM, JCL, BF, YLY

Competing Interests: Authors declare that they have no competing interests.

Materials and Correspondence: Correspondence and data requests should be sent to the corresponding author, Dr. Yuk L. Yung (yly@gps.caltech.edu).

References

1. Cicerone, R. J., & Oremland, R. S. (1988). Biogeochemical aspects of atmospheric methane. *Global Biogeochemical Cycles*, *2*(4), 299-327.
2. Yung, Y. L., Chen, P., Nealson, K., Atreya, S., Beckett, P., Blank, J. G., ... & Worden, J. (2018). Methane on Mars and habitability: challenges and responses. *Astrobiology*, 18(10), 1221-1242.
3. Oehler, D. Z., & Etiope, G. (2017). Methane seepage on Mars: where to look and why. *Astrobiology*, *17*(12), 1233-1264.
4. Oze, C., & Sharma, M. (2005). Have olivine, will gas: serpentinization and the abiogenic production of methane on Mars. *Geophysical Research Letters*, *32*(10).
5. Kite, E. S., Gao, P., Goldblatt, C., Mischna, M. A., Mayer, D. P., & Yung, Y. L. (2017). Methane bursts as a trigger for intermittent lake-forming climates on post-Noachian Mars. *Nature Geoscience*, *10*(10), 737-740.
6. Krasnopolsky, V. A., Maillard, J. P., & Owen, T. C. (2004). Detection of methane in the martian atmosphere: evidence for life?. *Icarus*, *172*(2), 537-547.
7. Formisano, V., Atreya, S., Encrenaz, T., Ignatiev, N., & Giuranna, M. (2004). Detection of methane in the atmosphere of Mars. *Science*, *306*(5702), 1758-1761.
8. Geminale, A., Formisano, V., & Giuranna, M. (2008). Methane in Martian atmosphere: average spatial, diurnal, and seasonal behaviour. *Planetary and Space Science*, *56*(9), 1194-1203.
9. Mumma, M. J., Villanueva, G. L., Novak, R. E., Hewagama, T., Bonev, B. P., DiSanti, M. A., ... & Smith, M. D. (2009). Strong release of methane on Mars in northern summer 2003. *Science*, *323*(5917),

1041-1045.

10. Fonti, S., & Marzo, G. A. (2010). Mapping the methane on Mars. *Astronomy & Astrophysics*, *512*, A51.
11. Krasnopolsky, V. A. (2012). Search for methane and upper limits to ethane and SO2 on Mars. *Icarus*, *217*(1), 144-152.
12. Aoki, S., Richter, M. J., DeWitt, C., Boogert, A., Encrenaz, T., Sagawa, H., ... & Fouchet, T. (2018). Stringent upper limit of CH4 on Mars based on SOFIA/EXES observations. *Astronomy & Astrophysics*, *610*, A78.
13. Giuranna, M., Viscardy, S., Daerden, F., Neary, L., Etiope, G., Oehler, D., ... & Cardesín- Moinelo, A. (2019). Independent confirmation of a methane spike on Mars and a source region east of Gale Crater. *Nature Geoscience*, *12*(5), 326-332.
14. Mahaffy, P. R., Webster, C. R., Cabane, M., Conrad, P. G., Coll, P., Atreya, S. K., ... & Mumm, E. (2012). The sample analysis at Mars investigation and instrument suite. *Space Science Reviews*, *170*(1), 401-478.
15. Webster, C. R., Mahaffy, P. R., Atreya, S. K., Flesch, G. J., Mischna, M. A., Meslin, P. Y., ... & Lemmon, M. T. (2015). Mars methane detection and variability at Gale crater. *Science*, 347(6220), 415-417.
16. Webster, C. R., Mahaffy, P. R., Atreya, S. K., Moores, J. E., Flesch, G. J., Malespin, C., ... & Vasavada, A. R. (2018). Background levels of methane in Mars' atmosphere show strong seasonal variations. *Science*, 360(6393), 1093-1096.
17. Korablev, O., Vandaele, A. C., Montmessin, F., Fedorova, A. A., Trokhimovskiy, A., Forget, F., ... & Vago, J. L. (2019). No detection of methane on Mars from early ExoMars Trace Gas Orbiter observations. *Nature*, 568(7753), 517-520.
18. Knutsen, E. W., Villanueva, G. L., Liuzzi, G., Crismani, M. M., Mumma, M. J., Smith, M. D., ... & Bellucci, G. (2021). Comprehensive investigation of Mars methane and organics with ExoMars/NOMAD. *Icarus*, 357, 114266.
19. Lefèvre, F., & Forget, F. (2009). Observed variations of methane on Mars unexplained by known atmospheric chemistry and physics. *Nature*, 460(7256), 720-723.
20. Moores, J. E., Gough, R. V., Martinez, G. M., Meslin, P. Y., Smith, C. L., Atreya, S. K., ... & Webster, C. R. (2019). Methane seasonal cycle at Gale Crater on Mars consistent with regolith adsorption and diffusion. *Nature Geoscience*, 12(5), 321-325.
21. Moores, J. E., King, P. L., Smith, C. L., Martinez, G. M., Newman, C. E., Guzewich, S. D., ... & Schuerger, A. C. (2019). The methane diurnal variation and microseepage flux at Gale crater, Mars as constrained by the ExoMars Trace Gas Orbiter and Curiosity observations. *Geophysical Research Letters*, 46(16), 9430-9438.
22. Gough, R. V., Tolbert, M. A., McKay, C. P., & Toon, O. B. (2010). Methane adsorption on a Martian soil analog: An abiogenic explanation for methane variability in the Martian atmosphere. *Icarus*, 207(1), 165-174.
23. Knak Jensen, S. J., Skibsted, J., Jakobsen, H. J., Inge, L., Gunnlaugsson, H. P., Merrison, J. P., ... & Nørnberg, P. (2014). A sink for methane on Mars? The answer is blowing in the wind. *Icarus*, 236, 24-

27.

24. Hu, R., Bloom, A. A., Gao, P., Miller, C. E., & Yung, Y. L. (2016). Hypotheses for near-surface exchange of methane on Mars. *Astrobiology*, 16(7), 539-550.
25. Mischna, M. A., Allen, M., Richardson, M. I., Newman, C. E., & Toigo, A. D. (2011). Atmospheric modeling of Mars methane surface releases. *Planetary and Space Science*, 59(2-3), 227-237.
26. Pla-García, J., Rafkin, S. C., Karatekin, Ö., & Gloesener, E. (2019). Comparing MSL Curiosity rover TLS-SAM methane measurements with Mars Regional Atmospheric Modeling System atmospheric transport experiments. *Journal of Geophysical Research: Planets*, 124(8), 2141-2167.
27. Lin, J. C., Gerbig, C., Wofsy, S. C., Andrews, A. E., Daube, B. C., Davis, K. J., & Grainger, C. A. (2003). A near-field tool for simulating the upstream influence of atmospheric observations: The Stochastic Time-Inverted Lagrangian Transport (STILT) model. *Journal of Geophysical Research: Atmospheres*, 108(D16).
28. Lin, J. C., D. Brunner, C. Gerbig, A. Stohl, A. K. Luhar, and P. W. Webley. (2012). Lagrangian Modeling of the Atmosphere. *Monogr.*, 200, 349.
29. Fasoli, B., Lin, J. C., Bowling, D. R., Mitchell, L., & Mendoza, D. (2018). Simulating atmospheric tracer concentrations for spatially distributed receptors: updates to the Stochastic Time-Inverted Lagrangian Transport model's R interface (STILT-R version 2). *Geoscientific Model Development*, 11(7), 2813-2824.
30. Fonseca, R. M., Zorzano-Mier, M. P., & Martín-Torres, J. (2018). Planetary boundary layer and circulation dynamics at Gale Crater, Mars. *Icarus*, 302, 537-559.
31. Richardson, M. I., Toigo, A. D., & Newman, C. E. (2007). PlanetWRF: A general purpose, local to global numerical model for planetary atmospheric and climate dynamics. *Journal of Geophysical Research: Planets*, 112(E9).
32. Christensen, P. R., Bandfield, J. L., Hamilton, V. E., Ruff, S. W., Kieffer, H. H., Titus, T. N., ... & Greenfield, M. (2001). Mars Global Surveyor Thermal Emission Spectrometer experiment: investigation description and surface science results. *Journal of Geophysical Research: Planets*, 106(E10), 23823-23871.
33. Putzig, N. E., Mellon, M. T., Kretke, K. A., & Arvidson, R. E. (2005). Global thermal inertia and surface properties of Mars from the MGS mapping mission. *Icarus*, 173(2), 325-341.
34. Lee, C., Lawson, W. G., Richardson, M. I., Anderson, J. L., Collins, N., Hoar, T., & Mischna, M. (2011). Demonstration of ensemble data assimilation for Mars using DART, MarsWRF, and radiance observations from MGS TES. *Journal of Geophysical Research: Planets*, 116(E11).
35. Toigo, A. D., Lee, C., Newman, C. E., & Richardson, M. I. (2012). The impact of resolution on the dynamics of the martian global atmosphere: Varying resolution studies with the MarsWRF GCM. *Icarus*, 221(1), 276-288.
36. Guzewich, S. D., Talaat, E. R., Toigo, A. D., Waugh, D. W., & McConnochie, T. H. (2013). High-altitude dust layers on Mars: Observations with the Thermal Emission Spectrometer. *Journal of Geophysical Research: Planets*, 118(6), 1177-1194.

37. Guzewich, S. D., Wilson, R. J., McConnochie, T. H., Toigo, A. D., Banfield, D. J., & Smith, M. D. (2014). Thermal tides during the 2001 Martian global-scale dust storm. *Journal of Geophysical Research: Planets*, 119(3), 506-519.
38. Newman, C. E., Gómez-Elvira, J., Marin, M., Navarro, S., Torres, J., Richardson, M. I., ... & Bridges, N. T. (2017). Winds measured by the Rover Environmental Monitoring Station (REMS) during the Mars Science Laboratory (MSL) rover's Bagnold Dunes Campaign and comparison with numerical modeling using MarsWRF. *Icarus*, 291, 203-231.
39. Newman, C. E., Baker, M. M., Banfield, D. J., Banks, M., Karatekin, O., Navarro, S., ... & Viudez-Moreiras, D. (2020, December). Using InSight Wind Data to Validate Atmospheric Models and Improve Predictions for Other Locations on Mars. In *AGU Fall Meeting 2020*. AGU.
40. Draxler, R. R., & Hess, G. D. (1998). An overview of the HYSPLIT_4 modelling system for trajectories. *Australian Meteorological Magazine*, 47(4), 295-308.
41. Stein, A. F., Draxler, R. R., Rolph, G. D., & Stunder, B. J. (2015). B., Cohen, MD, and Ngan, F.: NOAA'S HYSPLIT atmospheric transport and dispersion modeling system, *Bulletin of the American Meteorological Society*, 96, 2059-2077.
42. Hanna, S. R. (1984). Applications in air pollution modeling. In Atmospheric turbulence and air pollution modelling (pp. 275-310). Springer, Dordrecht.
43. Hébrard, E., Listowski, C., Coll, P., Marticorena, B., Bergametti, G., Määttänen, A., ... & Forget, F. (2012). An aerodynamic roughness length map derived from extended Martian rock abundance data. *Journal of Geophysical Research: Planets*, 117(E4).
44. Thomson, D. J. (1987). Criteria for the selection of stochastic models of particle trajectories in turbulent flows. *Journal of fluid mechanics*, 180, 529-556.

Figures

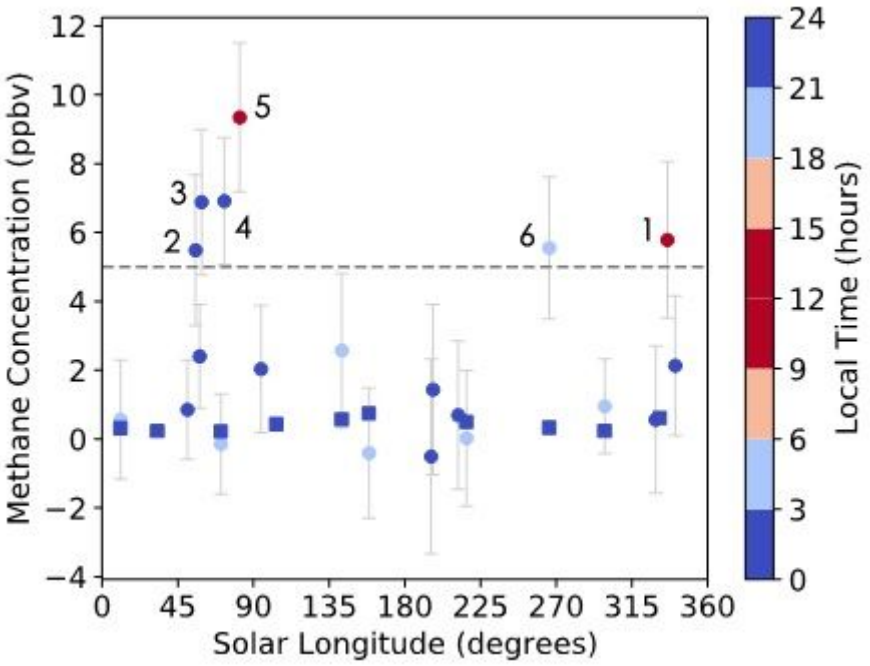

Figure 1

TLS methane signals versus Mars season. The six data points above the horizontal dashed line at 5 ppbv are the “methane spikes” with their indices next to them. The twenty-four data points below the dashed line are regarded as the background abundance. All the measurements were made in the nighttime except Spikes 1 and 5, which were measured in the early afternoon. Direct-ingest measurements are shown in circles. Enrichment measurements are shown in squares. Colors show the local time of ingestions. Error bars show ±1 standard error of the mean of each measurement. Adapted from ref. 16.

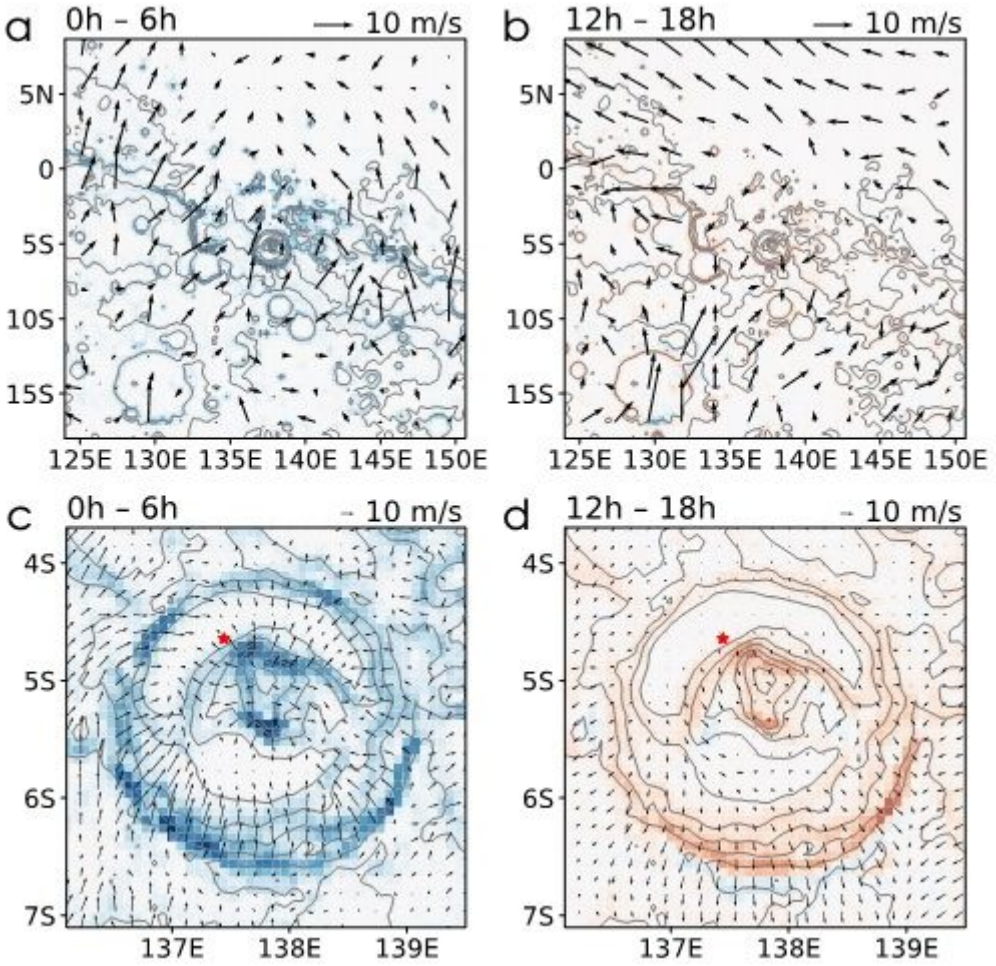

Figure 2

Simulated winds in the bottom layer of MarsWRF at 81.84° solar longitude (Spike 5). The plotted data is an average over six hours as indicated by the time period on the upper left of each panel. (a) and (b) show the regional circulation, from which one can identify southwesterly downslope winds along the topographic dichotomy from midnight to sunrise, and northeasterly upslope winds from noon to sunset. (c) and (d) show the Gale crater circulation, from which one can identify downslope winds along the inner wall of the crater rim and along Mount Sharp from midnight to sunrise, and upslope winds from noon to sunset. The crater circulation is resolved by MarsWRF. Red colors show rising air. Blue colors show sinking air. Contours show surface elevation. Red stars mark the position of Curiosity.

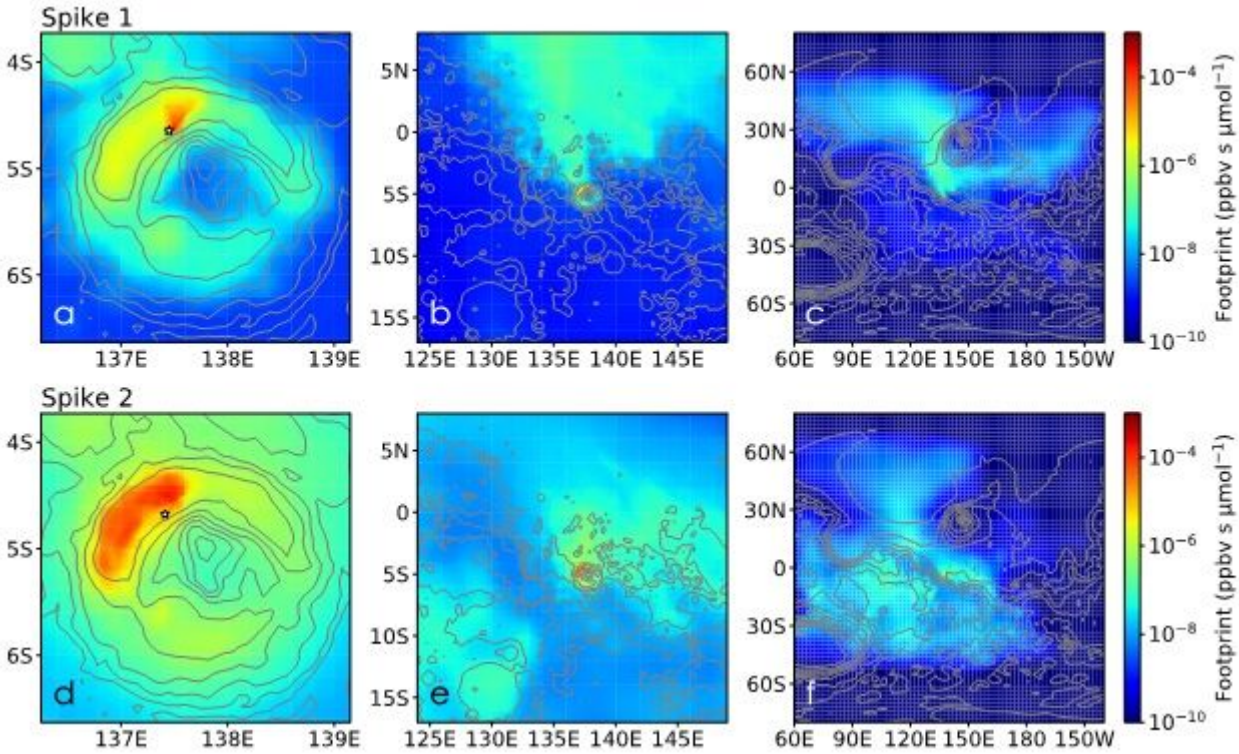

Figure 3

Influence of emission fluxes at any emission site on (a–c) Spike 1 and (d–f) Spike 2, shown in (a, d) the crater scale, (b, e) the regional scale, and (c, f) the hemispherical scale. Colors show STILT footprints integrated backwards in time over thirty sols. High values of footprints indicate upstream regions. The values of the footprints are equal to the prospected TLS methane signals in ppbv above the ~0.41 ppbv background after a thirty-sol constant-flux methane emission event with an emission flux of 1 µmol s-1 occurs at a single emission site. Stars in (a) and (d) mark the positions of Curiosity.

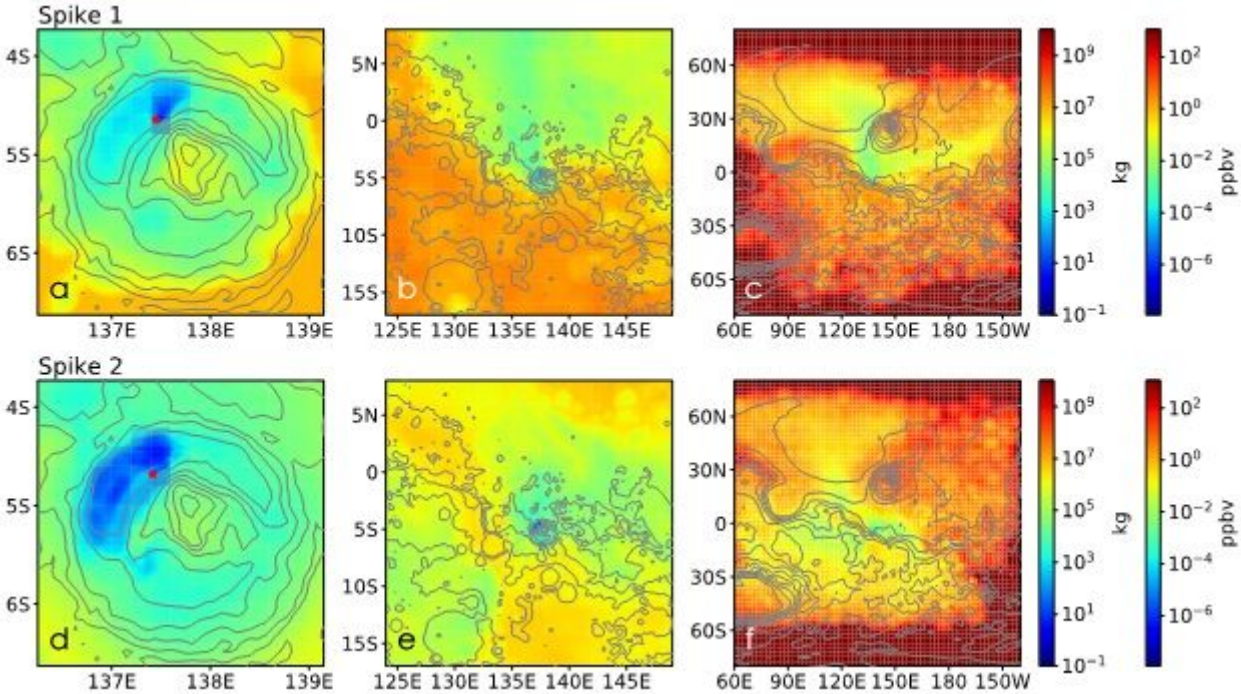

Figure 4

Minimum amount of emitted methane that can produce (a–c) Spike 1 and (d–f) Spike 2. The emission is assumed to occur at the moment when an emission site has the strongest influence on a detection. The second colorbar shows the rise in the global mean methane concentration after a minimum emission event. Stars in (a) and (d) mark the positions of Curiosity.

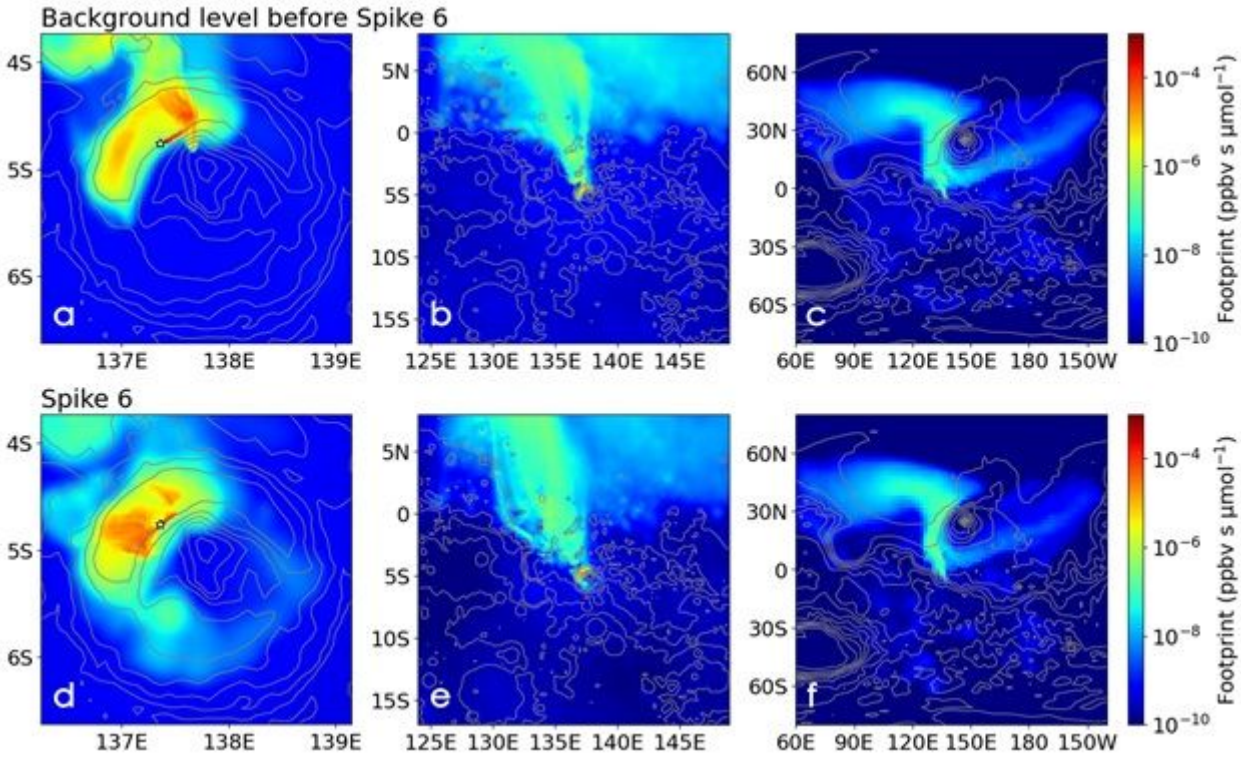

Figure 5

Comparison of the footprints for the background level and for Spike 6, both measured at ~266° solar longitude in Mars Year 33. Panels (a–c) show the STILT footprint for the background concentration. (d–f) show the STILT footprint for Spike 6. The stars in (a) and (d) show the positions of Curiosity. An emission site with weak influence on the background level and strong influence on Spike 6 will be bearing a small footprint for the former and a large footprint for the latter. Comparing (a) and (d), regions to the west and the southwest of Curiosity on the northwestern crater floor are such regions. The differences between (b) and (e) and between (c) and (f) at the larger scales are not significant.

Supplementary Files

This is a list of supplementary files associated with this preprint. Click to download.

- NatureCommunicationsmanuscriptsupplementary202105282058.pdf